photonics

MDPI

Article

High-Performance Normal-Incidence Ge/Si Meta-Structure Avalanche Photodetector

Jinwen Song [1], Shangwu Bin [1,*], Chaobiao Zhou [2] and Binyi Qin [1,3,4]

[1] School of Physics and Telecommunication Engineering, Yulin Normal University, Yulin 537000, China; jwsong@ylu.edu.cn (J.S.)
[2] College of Mechanical and Electronic Engineering, Guizhou Minzu University, Guiyang 550025, China
[3] Guangxi Colleges and Universities Key Laboratory of Complex System Optimization and Big Data Processing, Yulin Normal University, Yulin 537000, China
[4] Research Center of Intelligent Information and Communication Technology, Yulin Normal University, Yulin 537000, China
* Correspondence: binshangwu2012@163.com

Abstract: A high-speed and high-sensitivity avalanche photodetector (APD) is a critical component of a high-data-rate and low-power optical-communication link. In this paper, we study a high-speed and high-efficiency Ge/Si heterostructure APD. First, we numerically study the speed performance of the APD by analyzing frequency response. An optimized epitaxial structure of the high-speed APD is designed. In the absence of RC time effects, the APD exhibits a fast pulse response (full-width at half-maximum) of 10 ps and a high 3 dB bandwidth of 33 GHz at a high-gain value of 10. Taking device size and the corresponding RC time effects into account, the APD still achieves a high 3 dB bandwidth of 29 GHz at a gain value of 10. Moreover, a novel subwavelength periodic hole array is designed on the normal-incidence APD for enhancing light absorption without sacrificing speed performance. Near-perfect absorption is almost achieved by an infinite-period hole array due to the coupling of dual-resonance modes. A high-absorption efficiency of 64% is obtained by a limited-sized hole array in the high-speed APD. This work provides a promising method to design high-speed and high-efficiency normal-incidence Ge/Si heterostructure APDs for optical interconnect systems.

Keywords: Ge/Si heterostructure; avalanche photodetectors; optical resonance; high-speed

Citation: Song, J.; Bin, S.; Zhou, C.; Qin, B. High-Performance Normal-Incidence Ge/Si Meta-Structure Avalanche Photodetector. *Photonics* **2023**, *10*, 780. https://doi.org/10.3390/photonics10070780

Received: 13 June 2023
Revised: 30 June 2023
Accepted: 2 July 2023
Published: 4 July 2023

1. Introduction

In optical communications, a photodetector is the core component of a receiver to realize high-speed fiber optical links. Compared with conventional p-i-n photodetectors (PDs), APDs can provide higher sensitivity due to their internal gain, and are widely used in longer distance fiber transmission. However, the speed performances of APDs are usually poorer than the ones of PDs owing to the avalanche build-up time [1,2]. In order to decrease excess noise for high-speed APDs, selecting a material with low-ionization coefficient ratio as a multiplication layer is most important [3,4]. Silicon is well known for its low-ionization coefficient [5–7], which has great potential in high-performance APDs [8,9]. In a separate absorption, charge, and multiplication (SACM) structure, utilizing a Ge absorber can adapt Si APDs to operate at optical telecommunication wavelengths [10,11]. Ge/Si APDs have been studied a lot in the past dozen years [12–18], and have now emerged as a primary solution for optical-communication receivers [19,20]. Compared to high-performance III-V APDs, high-performance Ge/Si APDs are simpler in structure and compatible with CMOS fabrication.

Currently, the structures of Ge/Si APDs mainly include two kinds: waveguide and normal incidence. Waveguide photodetectors have the advantages of integration and high performance, while normal-incident photodetectors have the advantages of flexible application and cost efficiency. Unlike PDs, the avalanche build-up time of APDs will be the

main factor affecting the 3 dB bandwidth of the device at high gain, resulting in the similar speed performances between normal-incident APDs and waveguide APDs with a smaller RC constant [15,21]. However, normal-incident SACM Ge/Si APDs have lower primary responsivity [22], especially around 1550 nm [23,24]. In order to design high-performance normal-incident SACM Ge/Si APDs, a scheme of a SACM Ge/Si APD with high-speed and high-responsivity performance is presented in this paper, and the following areas are studied: (1) the main factors affecting the speed performance of SACM Ge/Si APDs; (2) light-absorption enhancement by a subwavelength periodic hole array.

The performances of Ge/Si APDs are mainly affected by the 3 dB bandwidth and responsivity of the devices. A typical SACM structure is adopted in the Ge/Si APD to achieve high speed with low noise. As shown in Figure 1b, photons are absorbed by the i-Ge layer, resulting in the generation of electron–hole pairs. Subsequently, the electrons move towards the i-Si layer and generate new electron–hole pairs within it by impact ionization. In the i-Si layer, the impact ionization of electrons and holes generates more electron–hole pairs, resulting in amplification of the current signal. In order to improve the speed performance of the APD, the thicknesses and doping concentrations of the epitaxial layers are analyzed in this work. A triple-mesa structure is designed to reduce the electric-field intensity in the edge of the Si-multiplication layer as shown as Figure 1a. At the center of the device, a subwavelength periodic hole array is designed to enhance light absorption by optical resonance.

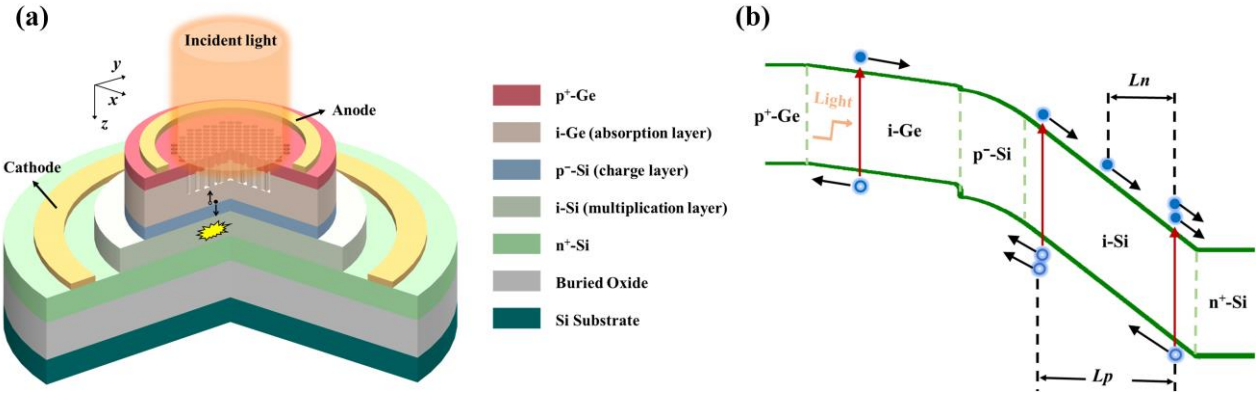

Figure 1. (**a**) Structure schematic of a SACM Ge/Si APD with a subwavelength periodic hole array. (**b**) The energy-band diagram of the SACM Ge/Si APD at operating bias. *Ln* (*Lp*) is the average distance an electron (hole) travels before ionizing, which is inversely proportional to the ionization coefficient of the electron (hole).

2. Analysis of the Effect of Epitaxial Layers and Device Size on Speed Performance

2.1. Methods

The optical–electrical conversion frequency response of the APD is determined by the time of free-carrier transport in the device (τ_{drift}), the avalanche build-up time (τ_{build}) and the external-parasitic RC time constant (τ_{RC}). The 3 dB bandwidth of a photodetector can be expressed as:

$$f_{3\mathrm{dB}} = \frac{1}{2\pi(\tau_{build} + \tau_{drift} + \tau_{RC})} = \frac{1}{2\pi(\tau_{carrier} + \tau_{RC})}. \quad (1)$$

Here, the sum of τ_{drift} and τ_{build} is called $\tau_{carrier}$. $\tau_{carrier}$ is determined by the weighted-average time that all free carriers take to be collected by the electrodes, starting from the generation of photo-generated carriers. The origin of the gain in an APD is impact ionization. However, the avalanche build-up time will rapidly increase while an APD is operating in gain mode, which is due to the collision, back and forth, of electrons and holes in the multiplication region. It means that τ_{build} will become a major factor influencing f_{3dB} while the APD is operating in high-gain mode. For high-speed APDs in high gain, a short

$\tau_{carrier}$ is important, which is mainly related to the thicknesses of the epitaxial layers and gain value. On the other hand, a short enough τ_{RC} is necessary, which mainly depends on the size of APDs.

In order to evaluate the effects of epitaxial layers, gain value, and device size on the frequency response of the Ge/Si APD, steady-state numerical simulations were performed for the device by using Silvaco ATLAS. The Parallel Electric Field Dependence, Selberherr's Impact Ionization models are used in our simulation. The impact-ionization model is based upon the following expressions:

$$G = \alpha_n J_n + \alpha_p J_p \tag{2}$$

and

$$\alpha_{n,p} = A_{n,p} \exp(-\frac{B_{n,p}}{E}). \tag{3}$$

Here, G is the generation rate of electron–hole pairs, and represents the number of generating electron–hole pairs per unit time and unit volume. The units of G are $cm^{-3} \cdot s^{-1}$. $\alpha_{n,p}$ are the ionization coefficients for electrons and holes, which represent the number of generating electron–hole pairs per unit distance of an electron or a hole under the influence of an electric field. The units of $\alpha_{n,p}$ are cm^{-1}. $J_{n,p}$ are their current flux densities, which represent the number of electrons or holes passing through a unit area per unit time. The units of $J_{n,p}$ are $cm^{-2} \cdot s^{-1}$. E is the magnitude of electric field, and the parameters $A_{n,p}$ and $B_{n,p}$ depend on the materials. The main parameters in our simulation are listed in Table 1.

Table 1. Material parameters used for Ge/Si APD simulation. The parameters from the references [25,26].

Parameters	Units	Electron	Hole
Saturated velocity of Si	cm/s	1.05×10^7	9.3×10^6
Impact coefficient A of Si	cm^{-1}	3.8×10^6	2.25×10^7
Impact coefficient B of Si	V/cm	1.75×10^6	3.26×10^6
Saturated velocity of Ge	cm/s	6×10^6	6×10^6
Impact coefficient A of Ge	cm^{-1}	5.9×10^5	2.6×10^5
Impact coefficient B of Ge	V/cm	7.9×10^5	7.1×10^5

2.2. Si-Multiplication Layer

To evaluate $\tau_{carrier}$ in the multiplication region, a pin-Si APD model was built, as shown as Figure 2a. In this model, the RC constant is set small enough to be negligible, resulting in $\tau_{RC} \approx 0$. By using the model, we calculated the frequency response of the devices with intrinsic layers of different thickness under different gain. An optical-pulse signal with 1 ps width was input into the pin-Si APDs, and the corresponding electrical-pulse signal was recorded at the same time, as shown in Figure 2b. The frequency response is obtained by a fast-Fourier transform (FFT) for the pulse response, as shown in Figure 2c.

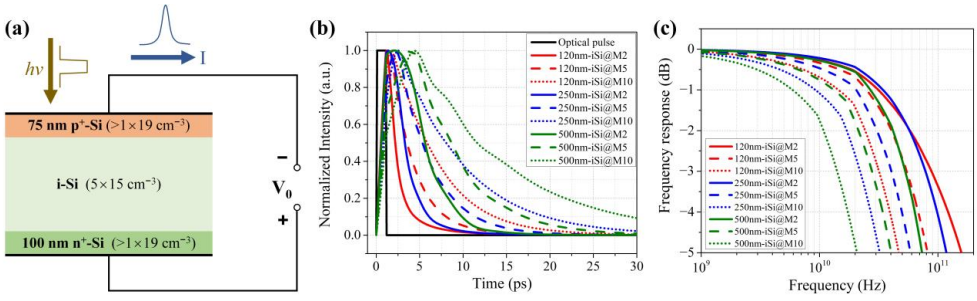

Figure 2. (**a**) The schematic diagram of the pin-Si APD model in our simulation. In the model, a 75 nm p^+-Si layer and a 100 nm n^+-Si layer are set, and the thickness of the i-Si layer is variable. (**b**) The simulated pulse response of the pin-Si APDs with i-Si layers of different thickness under different gain. (**c**) The corresponding frequency response of the devices.

Figure 2 shows the relationship between the pulse-response time of the i-Si layer and the gain value by changing the thickness of the Si-multiplication layer. It can be seen that the response time of the device increases as the thickness of the i-Si layer and the gain value increase. When the gain value is low (e.g., the multiplication factor M = 2), the avalanche build-up time is also short, and the response time is mainly determined by the i-Si thickness. With the increase of gain, the avalanche build-up time increases rapidly, resulting in a significant increase in the response time. No matter what size the photodetector, $\tau_{carrier}$ determinates the upper speed limit of the device. In Figure 2c, the 3 dB frequency responses at gain values of 2, 5, and 10 for the devices with i-Si-layer thicknesses of 500, 250, and 120 nm are as follows: 52, 28, and 14 GHz for 500 nm; 78, 40, and 22 GHz for 250 nm; and 88, 54, and 32 GHz for 120 nm. It can be seen that the 3 dB frequency response of the device with a thick multiplication layer is very low at high gain. For high-speed design, a high-frequency response is desired, and a thin Si-multiplication layer needs to be considered. On the other hand, a thinner Si-multiplication layer needs a stronger electric-field intensity to realize the same gain value. The tunnelling of the Si caused by high-electric-field intensity should be avoided for achieving a low-dark current. Based on the above consideration, we choose a 120 nm Si-multiplication layer for the design of the high-performance Ge/Si APD.

2.3. Charge Layer

In order to minimize the additional avalanche build-up time and carrier transit time, a thin charge layer with a thickness of 50 nm is chosen. Then, we discuss the design of the SACM structure as shown in Figure 1. The design mainly includes the thickness of the Ge-absorption layer, and the doping concentration of the charge layer.

As shown in Figure 3, the doping concentration of the p-Ge layer, the Ge-absorption layer, and n-Si layer are set as 1×10^{19}, 5×10^{15}, and 1×10^{20} cm^{-3}, and their thickness are 75, 300, and 100 nm, respectively. Figure 3 shows the electric-field distribution of the SACM Ge/Si APDs with different doping concentrations of charge layer under gain mode. With an increase in the doping concentration of the charge layer, the ratio of electric field between the multiplication layer and the absorption layer increases. The absorption layer needs sufficient electric-field intensity for the free carriers to reach saturation velocity, which is important for high-speed performance. It can be seen that the doping concentration of 7×10^{17} cm^{-3} is too high, resulting in insufficient electric-field intensity in the absorption layer. On the other hand, too high an electric field in the Ge-absorption layer isn't desired, because it will lead to a higher dark current owing to a trap-assisted-tunneling process [27]. It is better to design the electric-field intensity of the Ge-absorption layer to be below 1×10^5 V/cm. According to the calculation results in Figure 3, the doping concentration of the charge layer should be designed as a value near 5×10^{17} cm^{-3}.

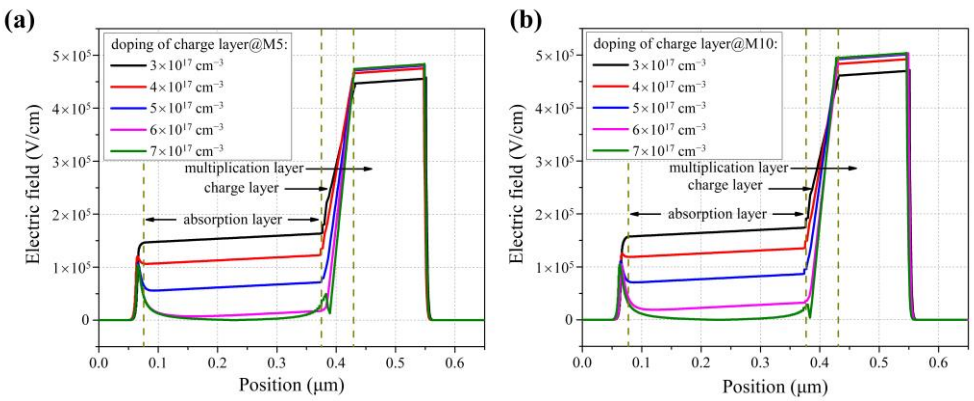

Figure 3. The electric-field distribution of the SACM Ge/Si APDs with different doping concentrations of charge layer. (**a**) The gain value is 5. (**b**) The gain value is 10.

2.4. Absorption Layer

Next, the design of the Ge-absorption layer is discussed. As shown in Figure 4a, a SACM Ge/Si APD model is built to calculate the carrier-transit time of the device. In this model, the RC constant is also set to be very small. In Figure 4, the analyzed method of time response and frequency response is the same as in the description of Figure 2. Using the model, the effect of the thickness of absorption layer on the frequency response is analyzed. The thickness of the Ge-absorption layer is set as 200, 300, and 400 nm, respectively. It can been seen that the response time of the SACM Ge/Si APD increases with an increase in the thickness of the absorption layer, owing to an increase in the carrier-transit time from the Ge-absorption layer. In Figure 4c, the 3 dB frequency responses at gain values of 2, 5, and 10 for the SACM Ge/Si APDs with Ge-absorption thicknesses of 200, 300, and 400 nm are as follows: 60, 51, and 39 GHz for 200 nm; 44, 39, and 33 GHz for 300 nm; and 34, 31, and 27 GHz for 400 nm. The device with a 400 nm absorption layer has a 3 dB frequency response of only 34 GHz even at low gain (M = 2). It means that the $\tau_{carrier}$ of the device has been dominated by the carrier-transit time rather than the avalanche build-up time from the Si-multiplication layer. As the thickness of the absorption layer decreases, the 3 dB frequency response of the device exceeds 30 GHz at M = 10. Because the free carriers enter the multiplication layer at the saturation velocity of the Ge layer, the 3 dB bandwidth of the SACM Ge/Si APD may exceed the value of the corresponding pin-Si APD at the same gain. On the other hand, decreasing the thickness of the absorption layer will decrease the optical responsivity of normal-incident photodetectors, which will decrease the sensitivity of the detectors. Therefore, the thickness of the absorption layer is set as 300 nm in the following design for high-speed APDs.

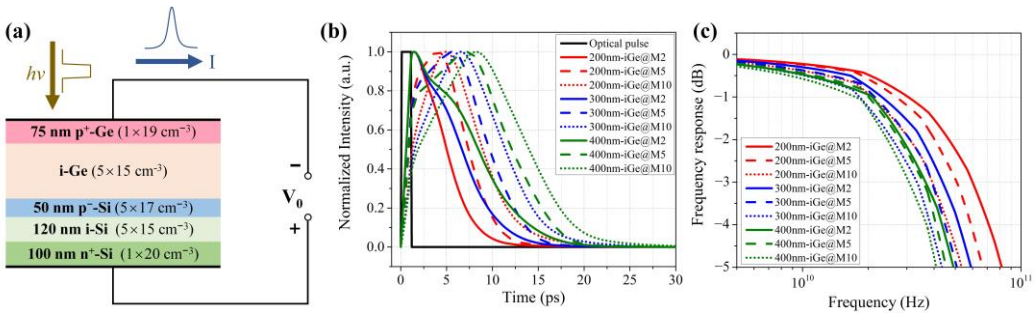

Figure 4. (**a**) The schematic diagram of the SACM Ge/Si APD model in our simulation. (**b**) The simulated-pulse response of the SACM Ge/Si APDs with i-Ge layers of different thickness under different gain. (**c**) The corresponding frequency response of the devices.

The influence of epitaxial layers and gain value on the frequency response of the Ge/Si photodetectors is discussed above. For clearer comparison, the 3 dB frequency responses of different devices without the effect of RC time are listed in Table 2. After considering the trade-off between speed and optical-responsivity performance, a 300 nm i-Ge and a 120 nm i-Si epitaxial layer are chosen for the high-speed SACM Ge/Si APDs in the subsequent design.

2.5. Size of Device

Figure 5 shows the effect of the size of the device on the 3 dB bandwidth under different gain. A three-mesa structure is designed to decrease the electric field on the edge of the multiplication layer [28], as shown as Figure 5a. Assuming that the device's top mesa is x microns in diameter, the second mesa is x + 4 microns, and the third one is x + 16 microns. The 3 dB bandwidths of the APDs are calculated as shown as Figure 5b. The calculation method is the same as for Figure 2 except that the RC constant of the device is considered here. In the calculation, a series resistance of 60 Ω is set, which includes a contact resistance of 10 Ω and a load resistance of 50 Ω. When x is set to 10, 12, 14, and 16, the capacitances of the APDs are about 22, 31, 42, and 55 fF, respectively. When the gain of

the APD is too high (e.g., M = 30), the avalanche build-up time becomes the key affecting the 3 dB bandwidth of the device, resulting in the 3 dB bandwidth of the device not varying with the RC constant. When the gain of the APD is below 10, the 3 dB bandwidth of the device can be significantly increased by reducing the size of the device. When x is 10 and 12, the 3 dB bandwidths of the APDs are up to 30 and 29 GHz at M = 10, which is close to the limit value of 33 GHz from Figure 4c. It means that further reduction in the device size hardly improves the APD's speed. Considering the fabrication complexity and the optical-window size of the APD, the better diameter of the top mesa would be more than 10 µm. More discussion about the current–voltage property of the APD is given in Supplementary Section SIII.

Table 2. The 3 dB frequency responses of different pin-Si APDs and SACM Ge/Si APDs without the effect of RC time.

Device Type	Thickness of Epitaxial Layer (nm)					3 dB Frequency Response (GHz) at Different Gain		
	p^+ Layer	i-Ge	p^--Si (5×10^{17} cm^{-3})	i-Si	n^+ Layer	M = 2	M = 5	M = 10
pin-Si APD	75	\	\	120	100	88	54	32
	75	\	\	250	100	78	40	22
	75	\	\	500	100	52	28	14
SACM Ge/Si APD	75	200	50	120	100	60	51	39
	75	300	50	120	100	44	39	33
	75	400	50	120	100	34	31	27

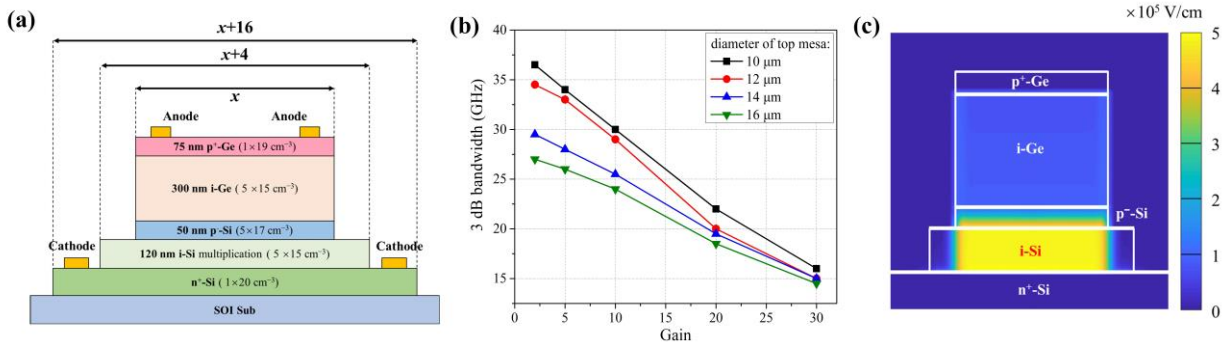

Figure 5. (**a**) The structure diagram of the SACM Ge/Si APD with three mesas. (**b**) The 3 dB bandwidth for the APDs with different sizes under different gain. (**c**) The electric-field profile at M = 10 for the APD with a top-mesa diameter of 12 µm.

3. Design of Light-Absorption Enhancement

In order to achieve high-speed performance, the absorption layer of the APD has to be as thin as 300 nm. However, a thin-absorption layer will result in low-optical responsivity of the device. In this part, the optical structure of the APD is optimized to improve the responsivity without sacrificing the high-speed performance. As shown in Figure 6a, a meta-structure consisting of a subwavelength periodic hole array is designed on the surface of the epitaxial layers. The top layer of the hole array is covered with a 430 nm SiO_2 passivation layer. The thicknesses of the n^+-Si and buried-oxide layers are 150 nm and 2 µm, and the thicknesses of other layers are the same as in Figure 5a.

The subwavelength period dielectric or metal structure can support abundant electromagnetic resonances. In the optical frequency, electromagnetic resonances can increase the photon lifetime and enhance the interaction between light and matter in the local fields. Such characteristics of the electromagnetic resonances have been employed in lasers [29,30], nonlinear-optical enhancement [31–33], perfect absorbers [34–38], and photodetectors [39–44]. Here, subwavelength periodic hole arrays are used to increase the light absorption of the APD by exciting optical-resonance modes.

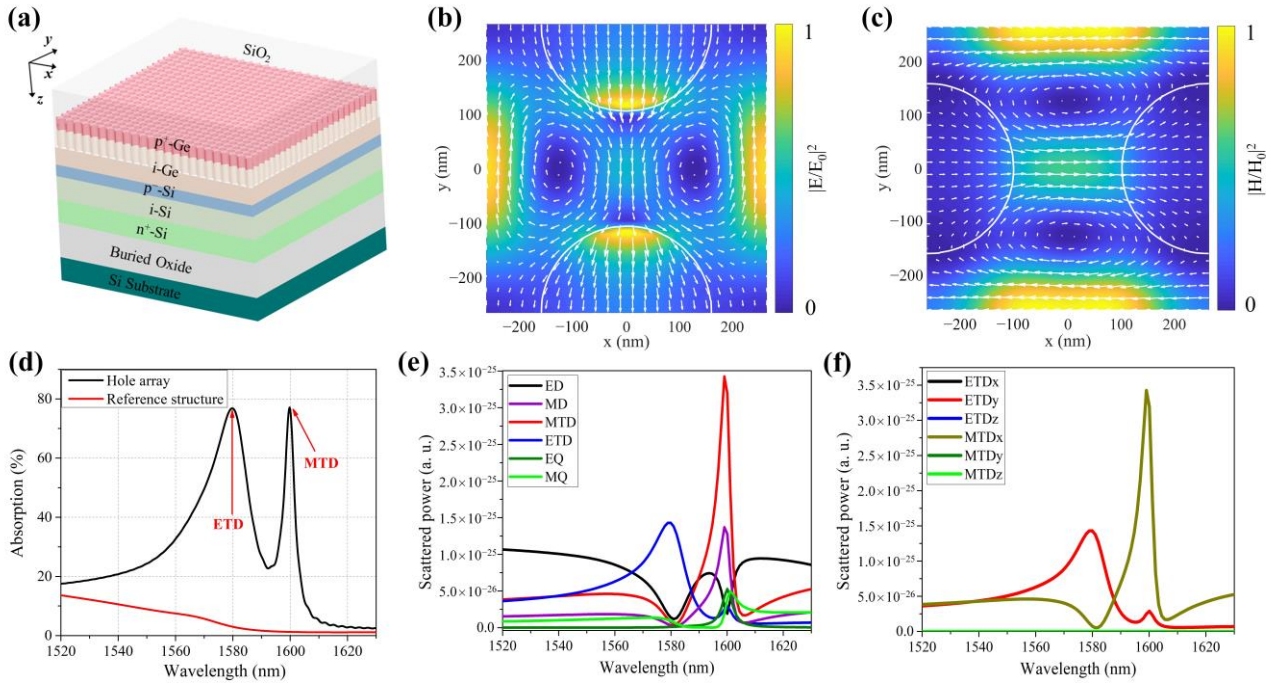

Figure 6. (**a**) The structure diagram of the periodic hole array on the surface of the epitaxial layer. (**b**) Near-field distributions of the electric-toroidal dipole (ETD) at the i-Ge cross section of the *x*-*y* plane. (**c**) Near-field distributions of the magnetic-toroidal dipole (MTD) at the i-Ge cross section of the *x*-*y* plane. (**d**) Calculated-absorption spectra of the hole array and the reference structure without hole array. (**e**) The scattering spectra of different multipoles. (**f**) The scattering spectra of the MTD and the ETD in the *x*, *y*, *z* directions, respectively.

The finite-difference time-domain (FDTD) method is used to analyze optical characteristics of the hole array, which is assumed to have an infinite number of periods with periodic boundary conditions. The purpose of this section is to optimize the light absorption of the APD in the C-band. First, the period, radius, and depth of the hole are adjusted to excite strong-resonance modes near 1550 nm. For illumination using a y-polarized plane wave at normal incident, the calculated-absorption spectra of a hole array and a reference structure without hole array are shown in Figure 6d.

The period, radius, and depth of the hole array are 530, 160, and 210 nm, respectively. Two absorption-enhancement peaks are obvious at 1580 and 1600 nm. It means that there are two optical-resonance modes at the same time, which are marked as mode I and mode II, respectively. The absorption of the two modes reached 76% and 77%, respectively. To understand the resonance characteristics of the two optical modes, Figure 6b,c shows the magnetic/electric-field intensity *x*-*y* profiles of mode I and mode II. It is seen that mode I is dominated by the ETD response, and mode II is the MTD response. This ETD response is created by a couple of mirror-symmetric vortex electric fields at the *x*-*y* plane, which can be viewed as a set of magnetic dipoles arranged head-to-tail to form a closed loop at the *x*-*z* plane [45,46]. Similarly, the MTD is created by a couple of mirror-symmetric vortex magnetic fields. To further analyze this resonance, electromagnetic-multipole expansion in Cartesian coordinates is performed [47–49]. The scattered powers of electric dipole (ED), magnetic dipole (MD), toroidal-electric dipole (TED), toroidal-magnetic dipole (TMD), electric quadrupole (EQD), and magnetic quadrupole (MQD) are calculated. It can be seen from Figure 6e that the resonances at 1580 and 1600 nm are mainly contributed by the MTD and ETD responses, respectively. Figure 6f shows that the MTD and ETD are mainly contributed by *y* and *x* directions, which are consistent with Figure 6b,c.

Optical-absorption properties of subwavelength periodic hole arrays are closely related to their period, radius, and depth. Next, a higher light absorption is obtained by changing the size of the hole array. Figure 7a shows the absorption spectrum of a hole array as

a function of its radius. As the radius changes, it is observed that the light absorption of the hole array is enhanced when the MTD and ETD modes start to overlap. When the radius is 210 nm, an approximate perfect absorption (97.2%) is obtained at 1550 nm, which is attributed to the coupling of ETD and MTD modes, as shown in Figure 7b. The absorption spectrum of the hole array as a function of its period and depth are provided in Supplementary Section SI. The results show good fabrication tolerance of the hole array to achieve high-light absorption. Figure 7c shows the electric-field *x*-*z* profiles in the middle of a hole cell at 1550 nm. It is seen that most energy of the incident light is confined in the Ge and Si layers. For silicon, the optical-communication band is transparent. Even if the incident light is confined to the Si layer, the light will eventually be coupled to the Ge layer and gradually absorbed. The light intensity in the Ge layer is concentrated in the middle of the i-Ge layer at 1550 nm, which is helpful for the extraction of photo-generated carriers. The APD with a hole array has wavelength tunability of peak-absorption enhancement. Furthermore, the parameters of the hole array are designed for absorption enhancement at 1310 nm, which are provided in Supplementary Section SII.

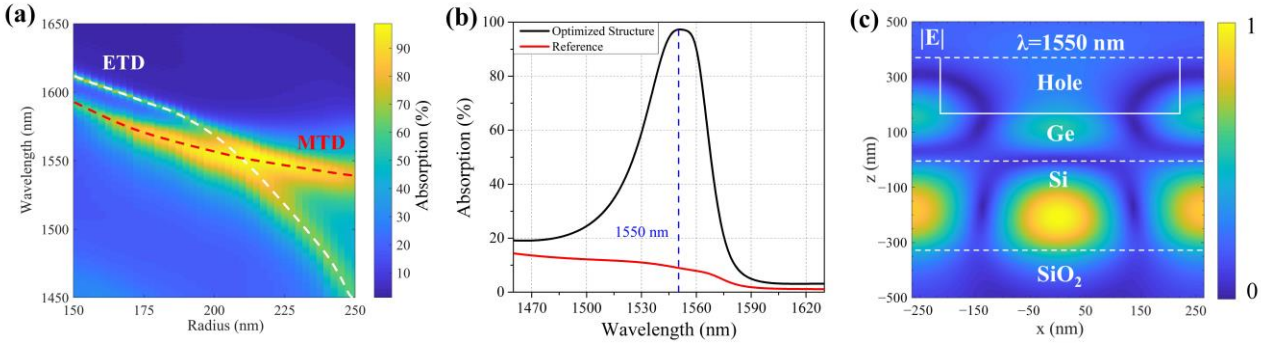

Figure 7. (**a**) Calculated-absorption spectrum of the hole array as a function of hole radius. The period and hole depth of the hole array are 530 and 210 nm. (**b**) Calculated-absorption spectra of the optimized hole array and the reference structure without hole array. The absorption peak of the hole array is 1544 nm, with a full-width at half-maximum (FWHM) of 48 nm. (**c**) The electric-field *x*-*z* profiles in the middle of a hole cell at 1550 nm.

In real application, the performance of a hole array with finite periods is more important than for one with infinite periods, due to the limited size of the APD. A *y*-polarized gaussian beam with waist radius of 3 μm is set in the simulation as shown as Figure 8a. The top layer of the hole array is covered with a 300 nm SiO_2 passivation layer. The period, hole radius, and depth of the hole array are set as 530, 210, and 210 nm, respectively. The hole array completely fills a circle with radius R_{border}. Figure 8b shows the absorption spectra of the hole arrays with different R_{border}. Before the hole array completely covers the gaussian beam, the absorption of the hole array increases quickly with the increase in R_{border}. When R_{border} reaches 4 or 5 μm, the absorption efficiency is 64.2% or 64.6% at 1550 nm, which approaches a maximum. Considering the space of the anode electrode, the hole array with $R_{border} = a$ μm can be fabricated on the top mesa with a radius of $a + 2$ μm, respectively. Comparing the results between Figures 5b and 8b, it is seen that the hole array with $R_{border} = 4$ μm is a better choice to realize high-speed and high-responsivity performance, as shown in Table 3.

In this part, a hole array is designed to enhance light absorption of the APD at 1550 nm. A high-absorption efficiency of 97.2% is obtained in the APD's epitaxial layer with only 300 nm i-Ge, which is about 10 times larger than that of a counterpart without the designed hole array. After considering the size limit of the hole array, the absorption efficiency will drop owing to optical-resonance weakening and lateral leakage. Finally, the absorption efficiency still reaches 64% at 1550 nm, which is compatible for a high-speed APD.

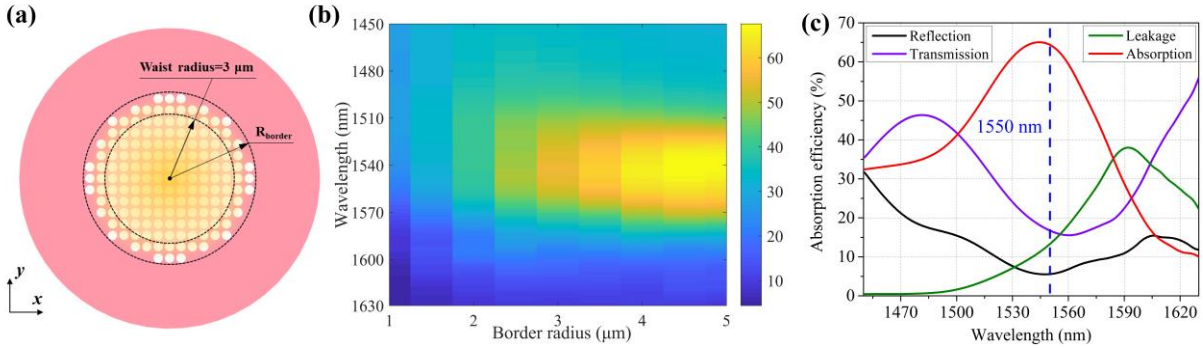

Figure 8. (**a**) The schematic of the hole array with finite periods in the simulation. The white circles are etched holes that completely fill a circle with radius R_{border}. (**b**) Calculated-absorption spectrum of the hole array as a function of R_{border}. (**c**) Calculated reflection, transmission, leakage, and absorption spectrum of the APD with R_{border} = 4 μm. The absorption peak of the APD is 1544 nm, with a FWHM of 134 nm.

Table 3. The optical absorption and speed performance of the SACM Ge/Si APDs with different size.

Diameter of Top Mesa (μm)	Maximum Optical-Absorption Efficiency at 1550 nm	3 dB Frequency Response (GHz) at Different Gain				
		M = 2	M = 5	M = 10	M = 20	M = 30
10	54.3%	36.5	34	30	22	16
12	64.2%	34.5	33	29	20	15
14	64.6%	29.5	28	25.5	19.5	14.5

4. Conclusions

In this work, we studied a high-performance normal-incidence SACM Ge/Si APD. The effects of the thicknesses and doping concentrations of the epitaxial layers, as well as the size of the device, on the 3 dB bandwidth of the device are analyzed under different gain values. We found that the avalanche build-up time of the APD decreases with the thinning of the multiplication layer at the same gain value. Appropriate Si-multiplication, charge, and absorption layers were designed for the high-speed performance of the APD. The APD achieved a 3 dB bandwidth of 29 GHz at M = 10 when the top-mesa diameter was 12 μm. Meanwhile, the optical structure of the device was optimized to enhance light absorption by a subwavelength periodic hole array, and the light absorption of the device at 1550 nm reached 64%. The APD can change peak-absorption enhancement by changing the size of the hole array. This work provides a promising method for the design of a high-performance normal-incidence Ge/Si APD, which has the potential to reduce the power consumption and cost of optical communications.

Supplementary Materials: The following supporting information can be downloaded at: https://www.mdpi.com/article/10.3390/photonics10070780/s1, Figure S1: The absorption spectrum of the hole array as functions of their period and depth; Figure S2: Design of hole array for absorption enhancement at 1310 nm; Figure S3: The current-voltage property of the SACM APD with a 12-μm-diameter top mesa.

Author Contributions: Conceptualization, J.S. and S.B.; methodology, J.S.; software, J.S. and S.B.; validation, J.S., S.B., C.Z. and B.Q.; formal analysis, J.S.; writing—review and editing, J.S. and S.B. All authors have read and agreed to the published version of the manuscript.

Funding: This work was supported by the Guangxi Provincial Science and Technology Projects (AD23026077, AD21238012), the National Natural Science Foundation of China (12004084, 12164008, 62041111), the Guizhou Provincial Science and Technology Projects (ZK[2021]030), the Natural Science Foundation of Guangxi Province (grant no.2019GXNSFBA245076).

Institutional Review Board Statement: Not applicable.

Informed Consent Statement: Not applicable.

Data Availability Statement: The data supporting the reported results can be obtained from the authors.

Conflicts of Interest: The authors declare no conflict of interest.

References

1. Emmons, R. Avalanche-photodiode frequency response. *J. Appl. Phys.* **1967**, *38*, 3705–3714. [CrossRef]
2. Teich, M.C.; Matsuo, K.; Saleh, B. Time and frequency response of the conventional avalanche photodiode. *IEEE Trans. Electron Devices* **1986**, *33*, 1511–1517. [CrossRef]
3. Campbell, J.C. Evolution of low-noise avalanche photodetectors. *IEEE J. Sel. Top. Quantum Electron.* **2021**, *28*, 1–11. [CrossRef]
4. McIntyre, R. Factors affecting the ultimate capabilities of high speed avalanche photodiodes and a review of the state-of-the-art. In Proceedings of the 1973 International Electron Devices Meeting, Washington, DC, USA, 3–5 December 1973; IEEE: New York, NY, USA, 1973; pp. 213–216.
5. Robbins, V.; Wang, T.; Brennan, K.; Hess, K.; Stillman, G. Electron and hole impact ionization coefficients in (100) and in (111) Si. *J. Appl. Phys.* **1985**, *58*, 4614–4617. [CrossRef]
6. Yeom, K.; Hinckley, J.M.; Singh, J. Calculation of electron and hole impact ionization coefficients in SiGe alloys. *J. Appl. Phys.* **1996**, *80*, 6773–6782. [CrossRef]
7. Lee, J.; Gutierrez-Aitken, A.; Li, S.; Bhattacharya, P. Responsivity and impact ionization coefficients of Si/sub 1-x/Ge/sub x/photodiodes. *IEEE Trans. Electron Devices* **1996**, *43*, 977–981.
8. Laforce, F. Low noise optical receiver using Si APD. In Proceedings of the Optical Components and Materials VI, SPIE, San Jose, CA, USA, 27–29 January 2009; pp. 293–304.
9. Huang, M.; Cai, P.; Li, S.; Hou, G.; Zhang, N.; Su, T.-I.; Hong, C.-Y.; Pan, D. 56GHz waveguide Ge/Si avalanche photodiode. In Proceedings of the 2018 Optical Fiber Communications Conference and Exposition (OFC), San Diego, CA, USA, 11–15 March 2018; IEEE: New York, NY, USA, 2018; pp. 1–3.
10. Kang, Y.; Liu, H.-D.; Morse, M.; Paniccia, M.J.; Zadka, M.; Litski, S.; Sarid, G.; Pauchard, A.; Kuo, Y.-H.; Chen, H.-W. Monolithic germanium/silicon avalanche photodiodes with 340 GHz gain–bandwidth product. *Nat. Photonics* **2009**, *3*, 59–63. [CrossRef]
11. Campbell, J.C. Recent advances in avalanche photodiodes. *J. Light. Technol.* **2016**, *34*, 278–285. [CrossRef]
12. Wang, B.; Mu, J. High-speed Si-Ge avalanche photodiodes. *PhotoniX* **2022**, *3*, 1–22. [CrossRef]
13. Kang, Y.; Huang, Z.; Saado, Y.; Campbell, J.; Pauchard, A.; Bowers, J.; Paniccia, M. High performance Ge/Si avalanche photodiodes development in Intel. In Proceedings of the Optical Fiber Communication Conference, Los Angeles, CA, USA, 6–10 March 2011; Optical Society of America: Washington, DC, USA, 2011.
14. Huang, M.; Li, S.; Cai, P.; Hou, G.; Su, T.-I.; Chen, W.; Hong, C.-Y.; Pan, D. Germanium on silicon avalanche photodiode. *IEEE J. Sel. Top. Quantum Electron.* **2017**, *24*, 1–11. [CrossRef]
15. Srinivasan, S.A.; Lambrecht, J.; Berciano, M.; Lardenois, S.; Absil, P.; Bauwelinck, J.; Yin, X.; Pantouvaki, M.; Van Campenhout, J. Highly sensitive 56 Gbps NRZ O-band BiCMOS-silicon photonics receiver using a Ge/Si avalanche photodiode. In Proceedings of the 2020 Optical Fiber Communications Conference and Exhibition (OFC), San Diego, CA, USA, 8–12 March 2020; IEEE: New York, NY, USA, 2020; pp. 1–3.
16. Yuan, Y.; Tossoun, B.; Huang, Z.; Zeng, X.; Kurczveil, G.; Fiorentino, M.; Liang, D.; Beausoleil, R.G. Avalanche photodiodes on silicon photonics. *J. Semicond.* **2022**, *43*, 021301. [CrossRef]
17. Xiang, Y.; Cao, H.; Liu, C.; Guo, J.; Dai, D. High-speed waveguide Ge/Si avalanche photodiode with a gain-bandwidth product of 615 GHz. *Optica* **2022**, *9*, 762–769. [CrossRef]
18. Liu, X.; Li, X.; Li, Y.; ZHi, Z.; Chen, B.; Hu, H.; Xie, Q.; Na, Q.; Li, X.; Guo, P. High-performance Cascaded surface-illuminated Ge-on-Si APD array. *IEEE Electron Device Lett.* **2022**, *44*, 205–208. [CrossRef]
19. Potet, J.; Simon, G.; Gaillard, G.; Dessemond, C.; Saliou, F.; Gay, M.; Chanclou, P.; Thual, M. Uncooled High Speed Ge/Si Avalanche Photodiode for 50 Gbit/s-PON with 60 km Reach. In Proceedings of the Optical Fiber Communication Conference, San Diego, CA, USA, 7–9 March 2023; Optica Publishing Group: Washington, DC, USA, 2023.
20. Wang, N.; Li, J.; Zhang, D.; Li, H.; Cheng, J.; Chen, W.; Mikhailov, V.; Inniss, D.; Chen, Y.; Duan, X. Real-Time 50Gb/s Upstream Transmission in TDM-PON with Class E1 Power Budget Using Ge/Si Avalanche Photodiode and Bismuth-Doped Fiber as Preamplifier. In Proceedings of the 2023 Optical Fiber Communications Conference and Exhibition (OFC), San Diego, CA, USA, 5–9 March 2023; IEEE: New York, NY, USA, 2023; pp. 1–3.
21. Shi, B.; Qi, F.; Cai, P.; Chen, X.; He, Z.; Duan, Y.; Hou, G.; Su, T.; Li, S.; Chen, W. 106 Gb/s normal-incidence Ge/Si avalanche photodiode with high sensitivity. In Proceedings of the 2020 Optical Fiber Communications Conference and Exhibition (OFC), San Diego, CA, USA, 8–12 March 2020; IEEE: New York, NY, USA, 2020; pp. 1–3.
22. Duan, N.; Liow, T.-Y.; Lim, A.E.-J.; Ding, L.; Lo, G. 310 GHz gain-bandwidth product Ge/Si avalanche photodetector for 1550 nm light detection. *Opt. Express* **2012**, *20*, 11031–11036. [CrossRef]
23. Ishikawa, Y.; Wada, K.; Liu, J.; Cannon, D.D.; Luan, H.-C.; Michel, J.; Kimerling, L.C. Strain-induced enhancement of near-infrared absorption in Ge epitaxial layers grown on Si substrate. *J. Appl. Phys.* **2005**, *98*, 013501. [CrossRef]

24. Liu, J.; Cannon, D.D.; Wada, K.; Ishikawa, Y.; Jongthammanurak, S.; Danielson, D.T.; Michel, J.; Kimerling, L.C. Tensile strained Ge p-i-n photodetectors on Si platform for C and L band telecommunications. *Appl. Phys. Lett.* **2005**, *87*, 011110. [CrossRef]
25. Sze, S.; Gibbons, G. Avalanche breakdown voltages of abrupt and linearly graded p-n junctions IN Ge, Si, GaAs, and GaP. *Appl. Phys. Lett.* **1966**, *8*, 111–113. [CrossRef]
26. Becker, J.; Fretwurst, E.; Klanner, R. Measurements of charge carrier mobilities and drift velocity saturation in bulk silicon of < 1 1 1> and < 1 0 0> crystal orientation at high electric fields. *Solid-State Electron.* **2011**, *56*, 104–110.
27. Chen, H.; Verheyen, P.; De Heyn, P.; Lepage, G.; De Coster, J.; Balakrishnan, S.; Absil, P.; Roelkens, G.; Van Campenhout, J. Dark current analysis in high-speed germanium pin waveguide photodetectors. *J. Appl. Phys.* **2016**, *119*, 213105. [CrossRef]
28. Li, B.; Lv, Q.-Q.; Cui, R.; Yin, W.-H.; Yang, X.-H.; Han, Q. A low dark current mesa-type InGaAs/InAlAs avalanche photodiode. *IEEE Photonics Technol. Lett.* **2014**, *27*, 34–37. [CrossRef]
29. Kodigala, A.; Lepetit, T.; Gu, Q.; Bahari, B.; Fainman, Y.; Kanté, B. Lasing action from photonic bound states in continuum. *Nature* **2017**, *541*, 196–199. [CrossRef] [PubMed]
30. Hirose, K.; Liang, Y.; Kurosaka, Y.; Watanabe, A.; Sugiyama, T.; Noda, S. Watt-class high-power, high-beam-quality photonic-crystal lasers. *Nat. Photonics* **2014**, *8*, 406–411. [CrossRef]
31. Yuan, S.; Wu, Y.; Dang, Z.; Zeng, C.; Qi, X.; Guo, G.; Ren, X.; Xia, J. Strongly enhanced second harmonic generation in a thin film lithium niobate heterostructure cavity. *Phys. Rev. Lett.* **2021**, *127*, 153901. [CrossRef]
32. Xu, L.; Kamali, K.Z.; Huang, L.; Rahmani, M.; Smirnov, A.; Camacho-Morales, R.; Ma, Y.; Zhang, G.; Woolley, M.; Neshev, D. Dynamic nonlinear image tuning through magnetic dipole quasi-BIC ultrathin resonators. *Adv. Sci.* **2019**, *6*, 1802119. [CrossRef]
33. Xu, L.; Smirnova, D.A.; Camacho-Morales, R.; Aoni, R.A.; Kamali, K.Z.; Cai, M.; Ying, C.; Zheng, Z.; Miroshnichenko, A.E.; Neshev, D.N. Enhanced four-wave mixing from multi-resonant silicon dimer-hole membrane metasurfaces. *New J. Phys.* **2022**, *24*, 035002. [CrossRef]
34. Saadabad, R.M.; Huang, L.; Miroshnichenko, A.E. Polarization-independent perfect absorber enabled by quasibound states in the continuum. *Phys. Rev. B* **2021**, *104*, 235405. [CrossRef]
35. Yu, J.; Ma, B.; Ouyang, A.; Ghosh, P.; Luo, H.; Pattanayak, A.; Kaur, S.; Qiu, M.; Belov, P.; Li, Q. Dielectric super-absorbing metasurfaces via PT symmetry breaking. *Optica* **2021**, *8*, 1290–1295. [CrossRef]
36. Chen, W.; Wang, X.; Duan, J.; Zhou, C.; Liu, T.; Xiao, S. Perfect absorption in free-standing GaAs nanocylinder arrays by degenerate critical coupling. *Opt. Mater.* **2021**, *121*, 111558. [CrossRef]
37. Tian, J.; Li, Q.; Belov, P.A.; Sinha, R.K.; Qian, W.; Qiu, M. High-Q all-dielectric metasurface: Super and suppressed optical absorption. *ACS Photonics* **2020**, *7*, 1436–1443. [CrossRef]
38. Huang, L.; Li, G.; Gurarslan, A.; Yu, Y.; Kirste, R.; Guo, W.; Zhao, J.; Collazo, R.; Sitar, Z.; Parsons, G.N. Atomically thin MoS2 narrowband and broadband light superabsorbers. *ACS Nano* **2016**, *10*, 7493–7499. [CrossRef]
39. Gansch, R.; Kalchmair, S.; Genevet, P.; Zederbauer, T.; Detz, H.; Andrews, A.M.; Schrenk, W.; Capasso, F.; Lončar, M.; Strasser, G. Measurement of bound states in the continuum by a detector embedded in a photonic crystal. *Light Sci. Appl.* **2016**, *5*, e16147. [CrossRef]
40. Liu, Z.; Liu, J.; Cheng, B.; Zheng, J.; Li, C.; Xue, C.; Wang, Q. Enhanced light trapping in Ge-on-Si-on-insulator photodetector by guided mode resonance effect. *J. Appl. Phys.* **2018**, *124*, 053101. [CrossRef]
41. Song, J.; Yuan, S.; Cui, C.; Li, Y.; Zeng, C.; Xia, J. Photonic crystal enabled manipulation of optical and electric field in germanium avalanche photodetectors. *Nanotechnology* **2021**, *32*, 145201. [CrossRef]
42. Saadabad, R.M.; Pauly, C.; Herschbach, N.; Neshev, D.N.; Hattori, H.T.; Miroshnichenko, A.E. Highly efficient near-infrared detector based on optically resonant dielectric nanodisks. *Nanomaterials* **2021**, *11*, 428. [CrossRef] [PubMed]
43. Song, J.; Yuan, S.; Cui, C.; Wang, Y.; Li, Z.; Wang, A.X.; Zeng, C.; Xia, J. High-efficiency and high-speed germanium photodetector enabled by multiresonant photonic crystal. *Nanophotonics* **2020**, *10*, 1081–1087. [CrossRef]
44. Chen, D.; March, S.D.; Jones, A.H.; Shen, Y.; Dadey, A.A.; Sun, K.; McArthur, J.A.; Skipper, A.M.; Xue, X.; Guo, B.; et al. Photon-trapping-enhanced avalanche photodiodes for mid-infrared applications. *Nat. Photonics* **2023**, *17*, 594–600. [CrossRef]
45. Kaelberer, T.; Fedotov, V.; Papasimakis, N.; Tsai, D.; Zheludev, N. Toroidal dipolar response in a metamaterial. *Science* **2010**, *330*, 1510–1512. [CrossRef] [PubMed]
46. Cui, C.; Yuan, S.; Qiu, X.; Zhu, L.; Wang, Y.; Li, Y.; Song, J.; Huang, Q.; Zeng, C.; Xia, J. Light emission driven by magnetic and electric toroidal dipole resonances in a silicon metasurface. *Nanoscale* **2019**, *11*, 14446–14454. [CrossRef]
47. Fu, T.; Zhou, Z.; Wang, D.; Yang, T.; Li, H.; Chen, Y. Electromagnetically induced transparency based on magnetic toroidal mode of dielectric reverse-symmetric spiral metasurfaces. *New J. Phys.* **2022**, *24*, 033024. [CrossRef]
48. Li, S.-Q.; Crozier, K.B. Origin of the anapole condition as revealed by a simple expansion beyond the toroidal multipole. *Phys. Rev. B* **2018**, *97*, 245423. [CrossRef]
49. Shi, Y.; Zhou, L.-M.; Liu, A.Q.; Nieto-Vesperinas, M.; Zhu, T.; Hassanfiroozi, A.; Liu, J.; Zhang, H.; Tsai, D.P.; Li, H. Superhybrid Mode-Enhanced Optical Torques on Mie-Resonant Particles. *Nano Lett.* **2022**, *22*, 1769–1777. [CrossRef] [PubMed]